Instant super-resolution imaging in live cells and embryos via analog image processing

Andrew G York[1], Panagiotis Chandris[2], Damian Dalle Nogare[3], Jeffrey Head[3], Peter Wawrzusin[1], Robert S Fischer[4], Ajay Chitnis[3] & Hari Shroff[1]

Existing super-resolution fluorescence microscopes compromise acquisition speed to provide subdiffractive sample information. We report an analog implementation of structured illumination microscopy that enables three-dimensional (3D) super-resolution imaging with a lateral resolution of 145 nm and an axial resolution of 350 nm at acquisition speeds up to 100 Hz. By using optical instead of digital image-processing operations, we removed the need to capture, store and combine multiple camera exposures, increasing data acquisition rates 10- to 100-fold over other super-resolution microscopes and acquiring and displaying super-resolution images in real time. Low excitation intensities allow imaging over hundreds of 2D sections, and combined physical and computational sectioning allow similar depth penetration to spinning-disk confocal microscopy. We demonstrate the capability of our system by imaging fine, rapidly moving structures including motor-driven organelles in human lung fibroblasts and the cytoskeleton of flowing blood cells within developing zebrafish embryos.

Modern fluorescence microscopy combines contrast, molecular specificity, speed and biocompatibility to enable the visualization of live cellular processes. Unfortunately, diffraction limits the resolution of a wide-field fluorescence microscope to ~250 nm laterally and 500–750 nm axially, and achieving even this 'diffraction-limited' performance is difficult in practice. Super-resolution imaging techniques[1] overcome this difficulty, yet speed, imaging duration and field of view are severely compromised in existing implementations, especially when compared to conventional microscopy. For example, single-molecule imaging[2,3] or stimulated emission depletion (STED) microscopy[4] enable spatial resolutions <100 nm over cellular areas but are limited to imaging speeds of ~0.01–1 Hz (with faster imaging trading field of view and image quality for speed)[5]. Neither single-molecule imaging nor STED is currently practical for time-lapse volumetric imaging, owing to the low acquisition speed and phototoxic illumination intensities (10^4–10^7 W/cm^2 peak intensities, tens of milliwatts average power).

In contrast to single-molecule imaging and STED, linear structured illumination microscopy[6,7] (SIM) provides a more modest resolution increase ($\sqrt{2}$-fold better than the diffraction limit, twofold better after deconvolution) but requires 10^3–10^6 lower illumination intensities, provides much faster acquisition rates (up to 11 Hz in 2D and 0.2 Hz in 3D)[8,9] and computationally rejects out-of-focus light. These advantages enable optically sectioned super-resolution imaging over hundreds of 3D time points in whole cellular volumes. The depth penetration of SIM can be further improved through the use of a sparse lattice of excitation points in combination with pinholes in the emission path and appropriate image processing[10–13] (**Supplementary Note**) to physically reject out-of-focus light, thus allowing live super-resolution imaging at depths ~50 μm from the coverslip surface[13] ('multifocal SIM' or MSIM). Regardless of the specific implementation, previous efforts have illuminated the sample with ~10–100 excitation patterns, acquired one camera exposure per pattern and digitally combined the resulting images to produce a single 2D super-resolution image. This need to capture and combine many raw images per plane has fundamentally limited the speed of SIM relative to conventional microscopy.

We report an analog implementation of structured illumination microscopy that doubles the spatial resolution of a fluorescence microscope, with no tradeoff in speed, phototoxicity or field of view. By eliminating the need to acquire and digitally combine multiple camera exposures, our method removes the only drawback of SIM compared to conventional fluorescence microscopy and permits super-resolution image acquisition and display in real time. Our technique allows multicolor volumetric imaging at rates comparable or faster than line-scanning or spinning-disk confocal microscopy, permitting two-color inspection of sub-mitochondrial detail otherwise obscured by diffraction or motion blur. We further highlight the advantage of our method relative to existing SIM implementations by performing noninvasive super-resolution imaging of interacting protein distributions at volumetric rates 15-fold faster than previously reported. Finally, we demonstrate super-resolution imaging at unprecedented speed by visualizing cytoskeletal detail within flowing blood cells *in vivo* (at 37 Hz) and capturing the millisecond-scale remodeling and growth of the endoplasmic reticulum (ER; at 100 Hz).

[1]Section on High Resolution Optical Imaging, National Institute of Biomedical Imaging and Bioengineering, National Institutes of Health, Bethesda, Maryland, USA. [2]National Institute of Diabetes and Digestive and Kidney Diseases, National Institutes of Health, Bethesda, Maryland, USA. [3]National Institute of Child Health and Human Development, National Institutes of Health, Bethesda, Maryland, USA. [4]National Heart, Lung, and Blood Institute, National Institutes of Health, Bethesda, Maryland, USA. Correspondence should be addressed to A.G.Y. (andrew.g.york+naturemethods@gmail.com).
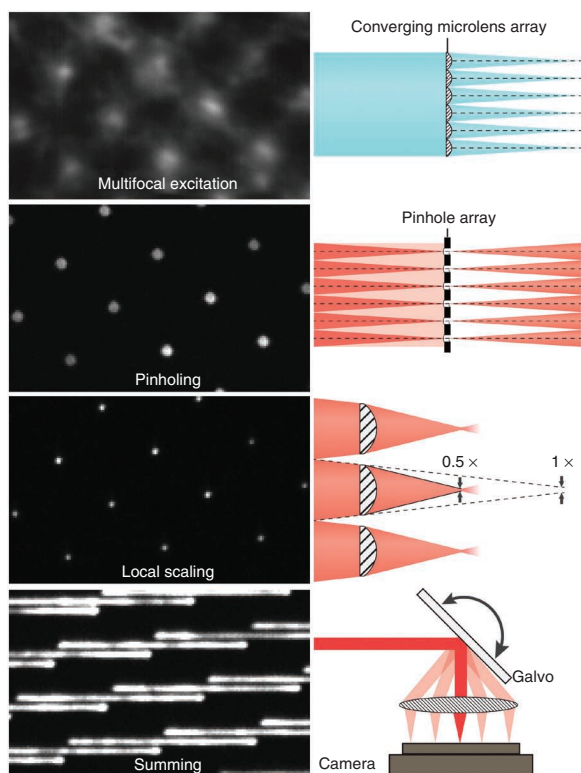
Figure 1 | Key steps in implementing instant structured illumination. A converging microlens array is used to produce a multifocal excitation. After exciting the sample, out-of-focus fluorescence is rejected with a pinhole array that is matched to the microlens array. A twofold local contraction of each pinholed fluorescence emission is achieved with the aid of a second, matched microlens array. A galvo serves to raster multifocal excitation and sum multifocal emission, producing a super-resolution image during each camera exposure (for clarity, only a partial galvo scan is shown). Left, raw data corresponding to each step. Right, cartoon representation (see also **Supplementary Fig. 1**).

Our instantaneous structured illumination microscope ('instant SIM'; **Supplementary Fig. 1–6**) directly captures optically sectioned images with √2-fold improvement in resolution in a single camera exposure and produces resolution-doubled images after a subsequent deconvolution step. As in MSIM, imaging Alexa Fluor 488–labeled microtubules in a fixed, human osteosarcoma (U2OS) cell with instant SIM revealed an apparent microtubule width of 150 nm, doubling wide-field resolution and allowing us to resolve microtubules with 110-nm center-to-center separation (**Supplementary Fig. 7**). We confirmed this result on 100-nm fluorescent beads (145 ± 14 nm (mean ± s.d.), $n = 10$), also obtaining the previously reported ~twofold increase in axial resolution (356 ± 37 nm) enabled by SIM (**Table 1** and **Supplementary Figs. 8** and **9**).

RESULTS

Analog image processing for instantaneous super resolution

The key realization underlying our approach is that every step of the digital combination in our previously described MSIM technique may be performed optically in an analog, effectively instantaneous fashion (**Supplementary Note**). MSIM data acquisition and processing may be conceptually divided into multiple steps: (i) sparse, multifocal illumination of the sample; (ii) recording the resulting fluorescence image with a camera; (iii) digital pinholing to reject out-of-focus emission; (iv) digital twofold contraction of each pinholed emission (without changing overall image dimensions); (v) repetition of steps (i–iv) at different positions of the multifocal excitation pattern until the entire field has been illuminated; (vi) digital summation of the resulting images to generate a super-resolution image with √2-fold improved resolution; (vii) deconvolution to recover the full twofold resolution improvement. Here we implement steps (i–vi) entirely in hardware (**Fig. 1**) using a microlens array to generate a multifocal excitation pattern, a matched pinhole array to reject out-of-focus emissions, a matched microlens array to locally contract each pinholed emission and a galvanometric mirror to translate the excitation pattern and sum the fluorescence emissions resulting from the three arrays before image collection and summation with a camera.

Rapid and noninvasive 3D super-resolution imaging

To demonstrate the capability of instant SIM for time-lapse interrogation of whole cellular volumes, we imaged a variety of dynamic protein distributions in transformed human lung fibroblasts. For example, we created a GFP chimera of TFAM, a mitochondrial DNA transcription factor that also acts to package mitochondrial DNA in nucleoids[14] and imaged it along with Tom20, a member of the translocase multimeric complex of outer mitochondrial membrane that functions to selectively transport proteins from cytosol into the mitochondrial intermembrane space, labeled with mCherry[15] (Tom20-mCherry) (**Fig. 2a** and **Supplementary Video 1**). The speed of instant SIM enabled us to collect each two-color, 3-µm-thick volume in 1.2 s (~15-fold faster than previous multicolor volumetric SIM on samples of equivalent thickness)[16], clearly resolving even fast-moving mitochondria that migrated at rates of 0.5–1 µm per second (**Fig. 2b**). Our resolution was sufficiently high to discern internal voids within most mitochondria (evident in the Tom20 channel, **Supplementary Fig. 10**). TFAM nucleoids (puncta sized at our resolution limit, in accordance with other super-resolution experiments on fixed cells)[17] were engulfed within mitochondrial voids (**Fig. 2b**), an observation confirmed in axial views of the sample (**Fig. 2c**). To our knowledge, STED is the only other super-resolution technique that has been used to reveal the absence of Tom20 from the inner

Table 1 | Apparent width of 100-nm subdiffractive beads, as measured in different microscopes

	Instant SIM, wide-field mode	Instant SIM Raw	Instant SIM + decon	SDC raw	SDC + decon	LSC raw	LSC + decon
NA	1.45	1.45	1.45	1.49	1.49	1.46	1.46
Lateral FWHM (nm)	281 ± 11	213 ± 26	145 ± 14	260 ± 11	188 ± 14	369 ± 30	250 ± 38
Axial FWHM (nm)	680 ± 30	511 ± 24	356 ± 37	633 ± 36	429 ± 20	661 ± 31	401 ± 14

Decon, deconvolution; NA, numerical aperture; SDC, spinning-disk confocal; LSC, line-scanning confocal; FWHM, full width at half maximum. 'Wide-field mode' measurements were conducted on the instant SIM with microlens arrays and pinholes removed. Beads appear sharpest in instant SIM, despite the lower NA. Data are means ± s.d. derived from 10 beads. 'Raw' values were taken as parameters for theoretical Gaussian point-spread functions (PSFs) used when deconvolving data sets used in this paper.
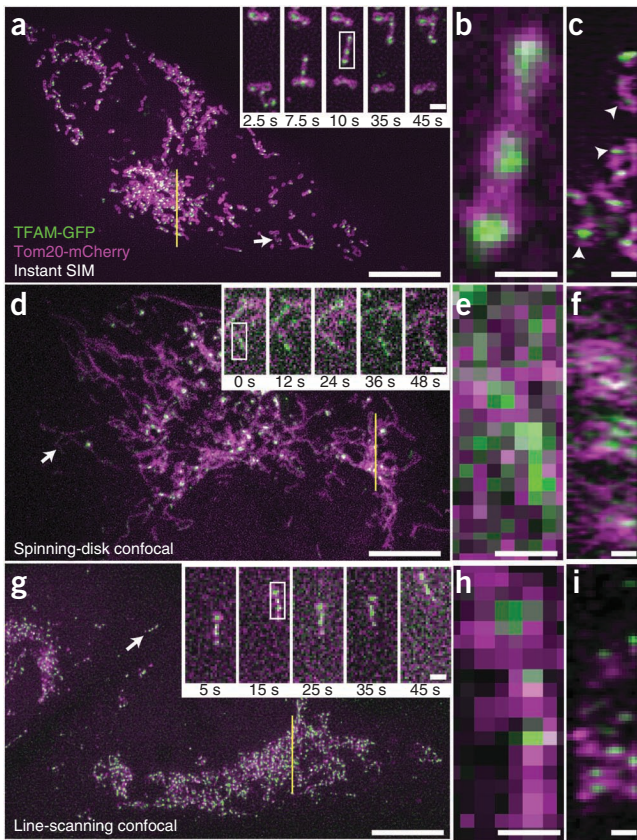
Figure 2 | Instant SIM enables high-speed two-color super-resolution imaging. (**a**–**i**) Live MRL-TR transformed human lung fibroblasts expressing TFAM-GFP (green) and Tom20-mCherry (magenta) were imaged in instant SIM (**a**–**c**), spinning-disk confocal (**d**–**f**) and a fast, line-scanning confocal microscope (**g**–**i**). Maximum-intensity projections (*xy*) of 3-µm-thick volumes are shown in **a**, **d** and **g** with subregions (white arrows) at indicated time points in higher magnification (inset). Line-scanning confocal inset in **g** has been rotated 90° relative to lower-magnification view. Scale bars, 10 µm and 1 µm (insets). Higher magnification of mitochondria are shown in **b**, **e** and **h** highlighted by white rectangles from insets in **a**, **d** and **g**. Scale bars, 0.5 µm. Axial (*zy*) views of ~270-nm-thick slices (yellow lines, **a**,**d**,**g**) are shown in **c**, **f** and **i**. White arrowheads indicate TFAM enclosed by Tom20 in instant SIM. Scale bars, 1 µm (see also **Supplementary Videos 1–3** and **Supplementary Figs. 8–12**).

and intracellular trafficking[20], over 60–100 imaging volumes (**Supplementary Videos 4** and **5**). Instant SIM revealed the formation and movement of tubular endosomes as well as highly mobile small vesicles in proximity to the basal membrane (**Supplementary Video 5**). In light of emerging interest on the interaction of peroxisomes with mitochondria[21], we performed live imaging of GFP-labeled peroxisomes in conjunction with Tom20-mCherry (**Supplementary Video 6**). Notably, our spatio-temporal resolution also allowed us to visualize rapid interactions of peroxisomes with mitochondrial spheroids (**Supplementary Video 7**). Finally, we used a GFP-labeled ER-peroxisome escort protein (GFP-SEC16B) and imaged its interactions with mCherry-labeled peroxisomes (**Supplementary Video 8**), observing 'kiss-and-run' interactions between these two partners, probably representing transfer of material from ER to peroxisomes[22] (**Supplementary Video 9**). In all cases, our acquisition rate was at least 15-fold faster than other SIM implementations[9,16].

Faster than video-rate super-resolution imaging

To fully exploit the speed of instant SIM, we recorded dynamics of the ER in a single 2D plane at 100 Hz over hundreds of time points (**Fig. 3a** and **Supplementary Video 10**). We chose the ER because of its highly plastic nature and rapid movement[23]. Our frame rate allowed easy observation and quantification of the
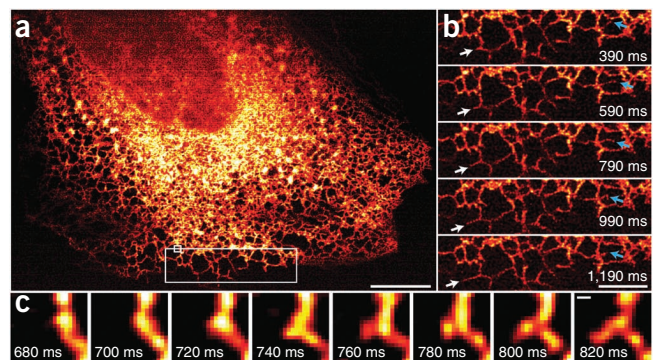
mitochondrial space[18,19], yet these experiments were performed on fixed cells, owing presumably to STED's slow acquisition speed or phototoxicity.

Functionally and conceptually, instant SIM is much like a spinning-disk confocal microscope with higher resolution, so we compared our method to this popular, proven technology. For two-color volumes of equivalent thickness, our spinning-disk system was ~10-fold slower than instant SIM (**Supplementary Video 2**), and both lateral and axial resolutions were worse than in instant SIM (**Fig. 2d–f**, **Table 1** and **Supplementary Figs. 8** and **9**). With (**Fig. 2e**) or without (**Supplementary Fig. 11**) deconvolution, the resolution of our spinning disk was insufficient to observe sub-mitochondrial voids (**Supplementary Fig. 12**) and blurred nucleoids enough that they often appeared as continuous, not discrete, entities (**Fig. 2e,f**). We also performed a comparison to a fast line-scanning confocal microscope that enabled imaging at similar volumetric acquisition rates to instant SIM (**Fig. 2g–i** and **Supplementary Video 3**). As with the spinning disk, mitochondrial voids were obscured (**Supplementary Fig. 12**), with (**Fig. 2h**) and without (**Supplementary Fig. 11**) deconvolution. Furthermore, the loss in axial resolution relative to instant SIM was enough that the enclosure of TFAM by Tom20 was completely masked by diffraction (**Fig. 2i**, **Table 1** and **Supplementary Figs. 8** and **9**).

The low intensities employed in instant SIM (~5–50 W/cm^2) allowed us to volumetrically image suitably bright samples over tens of time points without obvious photobleaching or signs of photodamage such as membrane retraction or blebbing. For example, we visualized the dynamics of abundant H-Ras and Rab8A GTPases, key players in growth factor signaling cascades

Figure 3 | Instant SIM reveals ER dynamics at 100 Hz. (**a**) First image in series of 200 time points, showing ER labeled with GFP-Sec61A within MRL-TR transformed human lung fibroblasts. Data were acquired at the coverslip surface. Scale bar, 10 µm. (**b**) Higher-magnification view of the large white rectangle in **a**. White arrows mark growth of an ER tubule; blue arrows indicate remodeling of an ER tubule. Scale bar, 5 µm. (**c**) Higher-magnification view of the small white rectangle in **a**, indicating formation of a new tubule within 140 ms. Scale bar, 200 nm (see also **Supplementary Video 10**).

Figure 4 | Imaging vascular flow with subcellular resolution at 37 Hz. Top, maximum-intensity projection across 100 2D frames (spanning 2,673 ms), highlighting GFP-labeled microtubules in blood cells located in cranial vessels, 20 μm into a 3-d-old zebrafish embryo. Direction of motion is left-right. Sharp cell boundaries indicate the absence of motion blur. Scale bar, 10 μm. Bottom, spatial regions corresponding to the red boxes (top) at indicated times. Yellow arrows, 'tail' structure at the end of the same cell; yellow arrowheads, microtubules feeding into tail; magenta arrowheads, microtubules present inside the cell. Scale bars, 2 μm (see also **Supplementary Video 11**).
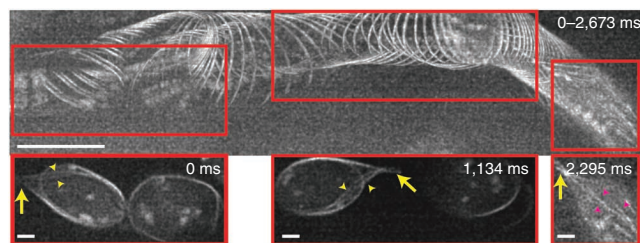
rapid growth (~3.5 μm per second) and remodeling of individual ER tubules (**Fig. 3b**). We also observed the formation and growth of new ER tubules, events that occurred in <140 ms (**Fig. 3c**) and that would have been blurred in any other SIM implementation, even at the very fastest 2D frame rates reported[8]. We note that our imaging rate is 50-fold faster than other methods that record ER dynamics at similar effective resolution[24], despite the 40-fold larger imaging area we cover.

An advantage of instant SIM is that its combination of computational and physical optical sectioning enables super-resolution imaging at sample depths ~10-fold deeper than possible with other SIM implementations[13]. We used this feature to image blood flow 20–25 μm from the coverslip surface, within cranial vessels of 3-d-old zebrafish embryos expressing a GFP transgene that labeled microtubules. Our imaging rate of 37 Hz was fast enough to 'freeze' individual blood cells, revealing subcellular detail despite their rapid movement (25 μm per second, **Fig. 4** and **Supplementary Video 11**). Some blood cells displayed 'tails' (**Fig. 4**) composed of multiple microtubules, in addition to intracellular microtubules that spanned the cell body. In some cases, microtubule bundles were splayed apart, revealing what are likely to be individual microtubules, as suggested by their sparse labeling. We speculate that the cells with tails may be neutrophils, as the tails are similar in appearance to 'sling' structures that help neutrophils roll in the presence of high shear forces[25], although the identity of these cells awaits confirmation.

DISCUSSION

Relative to previous forms of structured illumination microscopy that provide comparable resolution, optical sectioning, and depth penetration[13], instant SIM is 100-fold faster. Taking into account processing time, the speed-up factor exceeds 10,000. Owing to its near-instantaneous acquisition and display, instant SIM enables imaging at faster rates than those of state-of-the art commercial confocal microscopes and with better resolution. Relative to STED and single-molecule imaging techniques, instant SIM is orders of magnitude faster over comparable fields of view. Nevertheless, spatiotemporal resolution, light efficiency and depth penetration could be further improved.

Our 3D acquisition speed is limited by the inertia of our sample stage, but optical refocusing strategies[26] circumvent this problem and could enable higher volumetric frame rates. Our optical setup is reminiscent of a swept-field confocal system[27] with a single additional optical element (the microlens array in the emission path). This implies that commercial hardware might be easily modified to provide instant SIM capability, yet the correspondingly large number of optics in the emission path reduces signal levels and thus the maximum possible acquisition speed. We note that the multifocal excitation, pinholing and local contraction operations necessary in instant SIM might be performed

in a spinning-disk confocal geometry with many fewer emission optics, improving speed and signal levels accordingly. Using multifocal excitation necessarily implies a lower degree of optical sectioning than excitation with a single focused beam owing to pinhole cross-talk. Indeed, at the pinhole spacing we chose, instant SIM provided sectioning similar to spinning-disk confocal microscopy and inferior to point- or line-scanning confocal microscopy (**Supplementary Fig. 13**). Sectioning strength and depth penetration would be improved if pinholes were spaced farther apart or if multiphoton excitation were used. Finally, if fluorescence emission is made to depend nonlinearly on illumination intensity ('nonlinear SIM'), spatial resolution can be further increased[28,29], even over large fields of view and at sub-second frame rates[30]. The combination of photostable, reversibly switchable fluorescent proteins[24,31] with an instant SIM optical design may thus enable video-rate super-resolution imaging in the sub–100-nm regime.

METHODS

Methods and any associated references are available in the online version of the paper.

Note: Any Supplementary Information and Source Data files are available in the online version of the paper.

AUTHOR CONTRIBUTIONS
A.G.Y. and H.S. conceived idea and designed optical system. A.G.Y. built the optical system, designed and implemented data acquisition software and performed simulations. A.G.Y., P.C., D.D.N., J.H., R.S.F. and H.S. acquired data. P.C., D.D.N., R.S.F. and A.C. provided guidance on biological experiments. P.C., D.D.N., J.H., P.W. and R.S.F. prepared samples. P.C., D.D.N., J.H., R.S.F. and A.C. provided biological reagents. All authors analyzed data. A.G.Y., P.C. and H.S. wrote the paper with input from all authors. H.S. supervised research.

1. Hell, S.W. Far-field optical nanoscopy. *Science* **316**, 1153–1158 (2007).
2. Shroff, H., Galbraith, C.G., Galbraith, J.A. & Betzig, E. Live-cell photoactivated localization microscopy of nanoscale adhesion dynamics. *Nat. Methods* **5**, 417–423 (2008).

3. Jones, S.A., Shim, S.-H., He, J. & Zhuang, X. Fast, three-dimensional super-resolution imaging of live cells. *Nat. Methods* **8**, 499–505 (2011).
4. Westphal, V. *et al.* Video-Rate Far-Field Optical Nanoscopy Dissects Synaptic Vesicle Movement. *Science* **320**, 246–249 (2008).
5. Huang, F. *et al.* Video-rate nanoscopy using sCMOS camera-specific single-molecule localization algorithms. *Nat. Methods* **10**, 653–658 (2013).
6. Heintzmann, R. & Cremer, C.G. Laterally modulated excitation microscopy: improvement of resolution by using a diffraction grating. *Proc. SPIE* **3568**, 185–196 (1999).
7. Gustafsson, M.G.L. Surpassing the lateral resolution limit by a factor of two using structured illumination microscopy. *J. Microsc.* **198**, 82–87 (2000).
8. Kner, P., Chhun, B.B., Griffis, E.R., Winoto, L. & Gustafsson, M.G.L. Super-resolution video microscopy of live cells by structured illumination. *Nat. Methods* **6**, 339–342 (2009).
9. Shao, L., Kner, P., Rego, E.H. & Gustafsson, M.G.L. Super-resolution 3D microscopy of live whole cells using structured illumination. *Nat. Methods* **8**, 1044–1046 (2011).
10. Sheppard, C.J.R. Super-resolution in confocal imaging. *Optik* (*Stuttg.*) **80**, 53–54 (1988).
11. Müller, C.B. & Enderlein, J. Image scanning microscopy. *Phys. Rev. Lett.* **104**, 198101 (2010).
12. Heintzmann, R. & Benedetti, P.A. High-resolution image reconstruction in fluorescence microscopy with patterned excitation. *Appl. Opt.* **45**, 5037–5045 (2006).
13. York, A.G. *et al.* Resolution doubling in live, multicellular organisms via multifocal structured illumination microscopy. *Nat. Methods* **9**, 749–754 (2012).
14. Campbell, C.T., Kolesar, J.E. & Kaufman, B.A. Mitochondrial transcription factor A regulates mitochondrial transcription initiation, DNA packaging, and genome copy number. *Biochim. Biophys. Acta* **1819**, 921–929 (2012).
15. Baker, M.J., Frazier, A.E., Gulbis, J.M. & Ryan, M.T. Mitochondrial protein-import machinery: correlating structure with function. *Trends Cell Biol.* **17**, 456–464 (2007).
16. Fiolka, R., Shao, L., Rego, E.H., Davidson, M.W. & Gustafsson, M.G.L. Time-lapse two-color 3D imaging of live cells with doubled resolution using structured illumination. *Proc. Natl. Acad. Sci. USA* **109**, 5311–5315 (2012).
17. Brown, T.A. *et al.* Superresolution fluorescence imaging of mitochondrial nucleoids reveals their spatial range, limits, and membrane interaction. *Mol. Cell Biol.* **31**, 4994–5010 (2011).
18. Wurm, C.A. *et al.* Nanoscale distribution of mitochondrial import receptor Tom20 is adjusted to cellular conditions and exhibits an inner-cellular gradient. *Proc. Natl. Acad. Sci. USA* **108**, 13546–13551 (2011).
19. Schmidt, R. *et al.* Spherical nanosized focal spot unravels the interior of cells. *Nat. Methods* **5**, 539–544 (2008).
20. Mizuno-Yamasaki, E., Rivera-Molina, F. & Novick, P. GTPase networks in membrane traffic. *Annu. Rev. Biochem.* **81**, 637–659 (2012).
21. Neuspiel, M. *et al.* Cargo-selected transport from the mitochondria to peroxisomes is mediated by vesicular carriers. *Curr. Biol.* **18**, 102–108 (2008).
22. Yonekawa, S. *et al.* Sec16B is involved in the endoplasmic reticulum export of the peroxisomal membrane biogenesis factor peroxin 16 (Pex16) in mammalian cells. *Proc. Natl. Acad. Sci. USA* **108**, 12746–12751 (2011).
23. Woźniak, M.J. *et al.* Role of kinesin-1 and cytoplasmic dynein in endoplasmic reticulum movement in VERO cells. *J. Cell Sci.* **122**, 1979–1989 (2009).
24. Grotjohann, T. *et al.* rsEGFP2 enables fast RESOLFT nanoscopy of living cells. *eLIFE* **1**, e00248 (2012).
25. Sundd, P. *et al.* 'Slings' enable neutrophil rolling at high shear. *Nature* **488**, 399–403 (2012).
26. Botcherby, E.J., Juskaitis, R., Booth, M.J. & Wilson, T. Aberration-free optical refocusing in high numerical aperture microscopy. *Opt. Lett.* **32**, 2007–2009 (2007).
27. Brakenhoff, G.J. & Visscher, K. Confocal imaging with bilateral scanning and array detectors. *J. Microsc.* **165**, 139–146 (1992).
28. Rego, E.H. *et al.* Nonlinear structured-illumination microscopy with a photoswitchable protein reveals cellular structures at 50-nm resolution. *Proc. Natl. Acad. Sci. USA* **109**, E135–E143 (2012).
29. Gustafsson, M.G.L. Nonlinear structured-illumination microscopy: wide-field fluorescence imaging with theoretically unlimited resolution. *Proc. Natl. Acad. Sci. USA* **102**, 13081–13086 (2005).
30. Chmyrov, A. *et al.* Nanoscopy with more than 100,000 'doughnuts'. *Nat. Methods* **10**, 737–740 (2013).
31. Grotjohann, T. *et al.* Diffraction-unlimited all-optical imaging and writing with a photochromic GFP. *Nature* **478**, 204–208 (2011).

ONLINE METHODS

Instant SIM instrumentation. All optics were bolted to a 4 ft × 8 ft × 8 inch optical table (Newport) to minimize external vibrations. A rapid automated modular microscope (Applied Scientific Instrumentation, RAMM-FULL-INVAR) served as the microscope body that housed sample, objectives (Olympus, PlanApo, NA 1.45 TIRF, for single cells, or UPLSAPO 60XS, NA 1.3 silicone oil, for zebrafish embryos samples), and automated *xy* stage equipped with *z* axis piezo (Applied Scientific Instrumentation, PZ2300) that moved the axial position of the sample relative to the objective. For exciting fluorescence, two lasers were used: a 1 W, 488-nm laser and a 0.5 W, 561-nm laser (Coherent, Genesis MX488-1000 STM and Genesis MX561-500 STM). Lasers were combined via a dichroic mirror (DC, Semrock, LPD01-488RU-25) and passed through an acousto-optical tunable filter (AOTF, AA Optoelectronic, Quanta Tech, AOTFnC-400.650-TN) for shuttering control. The intensity of each laser was maximized by tuning the rotation of half-wave plates (Thorlabs, WPH10M-488 and AHWP05M-600) placed in front of each laser. After the AOTF, the beams were expanded 8.9× with a beam expander (Edmund, f = 45 mm, 64–837 and Thorlabs, f = 400, AC254-400-A), and passed through a converging microlens array (Amus, f = 1.86 mm, 1 mm thick, 25 mm diameter, antireflection coated over 400–650 nm, APO-Q-P222-F1.86), compensator plate (CVI Melles-Griot, PW1-2025-UV) and dichroic mirror 6 mm thick (TDC, Iridian Spectral Technologies, 488-561 DM). The compensator plate was used to cancel astigmatism that would otherwise arise when the focused beamlets passed through the tilted dichroic mirror. The resulting multifocal illumination was reimaged with a 1:1 telescope, consisting of two scan lenses (scan lens 1 and 2, Special Optics, f = 190 mm, 55-S190-60-VIS) placed in a 4f configuration. An additional demagnification of 116.7× was achieved by reimaging the resulting excitation to the sample plane with tube lens (Edmund, f = 350 mm, NT49-289-INK) and objectives (f = 3 mm), also placed in a 4f configuration, and aligned so that the rear focal plane of the tube lens coincided with the front focal plane of scan lens 2. Rotations of a two-sided galvanometric mirror (Galvo, Nutfield Technology, QS-12 Galvo-Based Single-Axis Scan Set, P-PWR15 (power supply), S-0152 (Connector Kit), 10-2564 (mounting block); and Sierra Precision Optics, SPO9086 Rev B X-Mirror, double-coated) placed midway between each scan lens served to translate the multifocal array at the sample plane, thus covering the imaging field.

Several of these optics were reused for emission, as fluorescence was collected along the same path, through objective, tube lens, scan lenses 1 and 2 and galvanometric mirror, before reflection from the 6-mm-thick dichroic mirror. Because the galvanometric mirror introduced an equal and opposite rotation angle on the return path ('descanning'), the multiple fluorescence foci produced at the focus of scan lens 1 were stationary. A pinhole array, with pinhole spacing equivalent to the spacing between microlenses in the converging microlens array (Photosciences, Chrome on 0.090-inch-thick quartz, pinhole spacing of 222 μm, pinhole diameter of 40 μm) placed at the front focal plane of scan lens 1 served to reject out-of-focus fluorescence emission present around each fluorescent beamlet. The resulting filtered beamlets were relayed to a secondary microlens array via a 1:1 imaging telescope (relay lenses, Thorlabs AC508-300-A-ML) and focused through a second microlens array (Amus, f = 0.93 mm, 1 mm thick, 25 mm diameter, antireflection coated over 400–650 nm, APO-Q-P222-F0.93) that locally contracted each fluorescent focus twofold, while preserving the orientation of each focus (see further discussion below and **Supplementary Fig. 3**). The locally scaled multifocal array thus produced was reimaged to a scientific-grade complementary metal-oxide semiconductor camera (PCO-TECH, pco.edge) via additional scan lenses (scan lenses 3 and 4, Special Optics, f = 190 mm, 55-S190-60-VIS) placed in a 4f configuration. By placing the galvanometric mirror at the midpoint between scan lenses, fluorescence was rescanned onto the camera, producing a super-resolution, sectioned image of the sample plane. A filter wheel (Sutter, FG-LB10-BIQ and FG-LB10-NW) and notch filters (Semrock, NF03-488E-25 and NF03-561E-25) placed immediately before the cameras served to reject excitation laser light. These optical elements are shown in **Supplementary Figure 1**.

Our magnification of 116.7× resulted in an imaging pixel size of 55.5 nm. Excitation power varied between 5 W/cm^2 and 50 W/cm^2 depending on the particular sample.

Placement of the second microlens array. In order to achieve a twofold local contraction of each fluorescent focus in the descanned path while retaining the orientation of each focus, we placed the second microlens array one focal length before the image that would have been produced by scan lens 3 had we not placed the second microlens array in the optical path. The justification for this choice can be derived mathematically starting from the Gaussian form of the thin-lens equation:

$$1/o + 1/i = 1/f$$

where o is the object position, i the image position, and f the focal length of the lens. The magnification $M = -i/o$.

We desire that $M = 0.5$, i.e., that the image of each fluorescent focus is a locally contracted but upright (noninverted) version of the focus before passage through the microlens array. Substituting $i = -0.5o$ in the lensmaker equation implies that $o = -f$ (the object is virtual, placed one focal length away from the microlens array on its downstream side) and $i = 0.5f$ (the image is formed 0.5f from the microlens array, on the same side as the object). A geometric proof is presented in **Supplementary Figure 3**.

Brightfield imaging. The instant SIM produces an optically sectioned fluorescence image at the camera, but we often found it useful to acquire wide field (nonsectioned) brightfield images for scouting purposes. We implemented brightfield imaging by illuminating the sample from above with a lamp (Danray Products LMP-24M) and directing the transmitted light to the camera with removable mirrors (Thorlabs, MFF001), bypassing most of the optics in the fluorescence path (**Supplementary Fig. 2**).

Alignment of instant SIM optics. Most optics in **Supplementary Figure 1** are straightforward to align. The most sensitive alignment involves finding the correct rotation angle of the emission path microlens array about the optical axis. The instant SIM 'paints' a 2D image with a 1D scan of a 2D grid of illumination points, so the angle between the grid axes and the scan direction is crucial for uniform illumination of the image. Small rotations (barely mechanically perceptible) of the emission path microlens

array from its optimal position can cause substantial striping artifacts in our images. In practice, we find the best alignment procedure is to image a thin, uniform fluorescent solution while carefully adjusting the rotation angle of the emission path microlenses and inspecting the resulting images for striping. The emission path pinholes and the excitation microlenses can then be (re)aligned to the emission path microlenses as required, as all three of these optics are mounted on removable magnetic stages (Thorlabs, KB3X3). One aligned, the system is stable and maintenance-free.

Instant SIM instrument control and data acquisition. Our previous MSIM implementation[13] controlled data acquisition with a custom Python script, but relied on manufacturer-supplied software and manual adjustment of hardware for exploring samples and identifying regions of interest. This is simple to implement and allows high-performance acquisition but requires well-trained users and often leads to substantial bleaching of the sample during the scouting process. The instant SIM is substantially faster, and a unified graphical interface was essential for taking full advantage of the device's capability for real-time super-resolution while minimizing sample perturbation. The instant SIM hardware is computer-controlled using custom software (**Supplementary Software**) written in the Python language[32] (http://www.scipy.org/) and is freely available at http://code.google.com/p/msim/.

We implemented graphical controls using the built-in Python library Tkinter. Image data are displayed in real time, on screen using the Python library pyglet (http://www.pyglet.org/). 3D volume data and time lapses are saved to disk as TIF files and automatically opened in ImageJ (http://rsb.info.nih.gov/ij/) as virtual stacks. We controlled the pco.edge camera using a manufacturer-supplied DLL and the built-in Python library ctypes. The Sutter filter wheel is controlled through a virtual serial port over USB, and the *x* and *y* positions of the ASI stage and the *z* position of the ASI objective stepper motor are interrogated through a physical serial port. Both the virtual and physical serial ports are controlled using the Python library pyserial (http://pyserial.sourceforge.net/). The galvanometric mirror, AOTF, piezo stage, bright-field bypass mirrors, and trigger signals to the PCO camera are all controlled by external voltages. A 16-channel analog-out card (National Instruments, NI 9264) provides these voltage signals, and is controlled through a manufacturer-supplied DLL and the Python ctypes library. The camera and the AOTF have low input impedance. The analog-out card specifications lead us to believe that it could drive enough current to work with this impedance, but in practice we found this false. We thus built a buffer amplifier using an op-amp, box and power supply (Radio Shack) to provide enough current to drive the camera, two channels of the AOTF and the AOTF blanking input.

High-speed operation of the instant SIM requires careful optimization of control voltages. **Supplementary Figure 4** shows an example of control voltages for a five-time-point, two-color time-lapse acquisition. Several features of these voltage signals are worth noting:

1. Even in the fully 'off' state, the AOTF still transmits a non-negligible fraction of the excitation laser, so between acquisitions, we leave the galvo mirror 'parked' in a highly deflected position to protect the sample from unnecessary phototoxicity. The 'unparking' of the galvo takes the longest time, so this occurs first.

2. We operate the pco.edge camera in 'rolling shutter' mode, which provides lower noise and higher speed relative to 'global shutter' mode. However, in rolling shutter mode, a lag exists between the external trigger signal and the moment when the entire camera chip is exposing. This lag is shorter than the galvo 'unparking' time, so it occurs next.

3. The galvanometric mirror vibrates if it scans too slowly, causing a substantial striping artifact in image data. For this reason, we only tune galvo scan speed over a narrow range, and implement longer exposures by accumulating several sweeps of the galvo. In **Supplementary Figure 4**, the galvo executes three sweeps per exposure. Between exposures, the galvo waits in a deflected position for whatever operation is the limiting factor. In this case, the rolling-shutter mode time lag is the limiting factor between time points.

4. The 488 and 561 lasers alternately illuminate the sample, providing fast two-color 2D time-lapse operation. All our experiments (as illustrated in **Supplementary Fig. 4**) used maximally permissive notch emission filters that eliminate 488-nm and 561-nm excitation light while transmitting all other wavelengths. This combination of filters works well for probes that may be distinguished by excitation alone, such as GFP and mCherry at similar probe density. A sample brightly tagged with tdTomato and weakly tagged with GFP might show substantial cross-talk between channels and require switching between two band-pass filters for each time point. The filter wheel we used has reasonably fast switching time (~10–50 ms), but switching between filters would still slow acquisition substantially.

Supplementary Figure 5 shows an example of control voltages for a four-slice, two-color *z*-stack. Voltages are similar to the 2D two-color time lapse, with a few differences:

1. The *z*-axis piezo stage control voltage is no longer constant. The piezo can be controlled through the serial port or an external voltage, but we found the external voltage control faster and more precise. The manufacturer specifies that a 5 V signal will move the piezo to the same position as a serial port command of '0', but we found the required '0' signal to be 5.08 V. It is unclear whether this difference is due to the *z* axis piezo or our analog-out card.

2. The limiting factor between time points alternates between the rolling shutter mode time lag, and the time period we allow for axial motions of the *z* piezo stage. We allow a ~10-ms delay for stage motion. Moving the piezo stage this rapidly requires careful optimization of the voltage waveform, as we found that fast movements of the piezo would otherwise cause substantial vibration with a resonant period of ~7.5 ms. A naive approach might be to simply move the piezo and wait for vibration to damp out, but we found that this takes many tens of milliseconds and would thus limit the speed of our *z* stacks. An improved approach might be to feed the piezo stage a smoothed signal to reduce vibration, but we found this still leads to unacceptable vibration over many resonant periods. The best approach we found applies three voltage steps per *z* piezo motion. **Supplementary Figure 6** shows a magnified view of our piezo control voltage.

The first voltage step overshoots the desired position, causing faster motion of the stage but also substantial vibration. The second voltage jump overshoots even further, and causes further vibration. However, these two motions are separated by half of the resonant vibration period, so the vibrations largely cancel each other out. The last voltage jump brings us back to the desired voltage,

separated by another half-resonant period. We experimented with various jump amplitudes and found the fastest motion with least vibration resulted when the first jump was twice as large as the desired motion, the second jump takes the stage to 2.4× the desired motion, and the final jump returns the stage to the desired position. The combination of voltage overshoot and vibration cancellation allows us to move the stage rapidly and precisely in just over one resonant vibrational period.

All volumes presented in this paper contained 12 imaging planes, with 0.25 µm spacing between planes.

Deconvolution. Although the raw images produced by instant SIM already possess improved resolution relative to conventional wide-field fluorescence images, achieving the full twofold resolution gain in SIM requires deconvolution.

For all 3D deconvolution (**Fig. 2** and **Supplementary Videos 1–9**), we used the Richardson-Lucy algorithm[33,34], assuming a symmetrical PSF:

For $i = 1, 2,…N$

$$New\_estimate = Previous\_estimate \times Blur\left(\frac{Measured\_image}{Blur(Previous\_estimate)} \right)$$

where $Blur()$ indicates convolution with the PSF. We assumed theoretical Gaussian PSFs with lateral and axial FWHMs derived from measurements on 100-nm yellow-green beads (**Table 1** lists the parameters used for instant SIM, line-scanning confocal and spinning-disk confocal images) and ran each deconvolution for 40 iterations. For 2D deconvolution, we used the Huygens deconvolution software (Scientific Volume Imaging) which seemed to give better results than our deconvolution algorithm. For deconvolving ER data sets (**Fig. 3**), we used the following parameters: 'confocal' PSF type, 55.5-nm pixel dimensions, 1.45 NA objective, 1.51 immersion oil index of refraction, 1.33 index of refraction of the imaging media and 40 iterations. For deconvolving fish-embryo data sets (**Fig. 4**), we used the following parameters: 'confocal' PSF type, 55.5-nm pixel dimensions, 1.3 NA objective, 1.4 immersion oil index of refraction, 1.33 index of refraction of the imaging media and 40 iterations. It is unclear what the Huygens processing algorithm is, but we suspect it is Richardson-Lucy deconvolution with pre-smoothing and a regularization step.

Image display. All movies were bleach-corrected using an ImageJ plugin (http://www.embl.de/eamnet/html/bleach_correction.html) that normalized the intensity values in each image to the average intensity present in that image.

For **Figure 3**, images were displayed using the 'HotRed' lookup table for ImageJ. All other images are presented in gray scale.

Molecular biology and cloning procedures. To label peroxisomes we replaced the mTurqoise2 fragment with the GFP or Cherry fragment between NheI and BsrGI in frame in the peroxisome targeting vector[35] (Addgene). ER was labeled with two constructs marking either the whole ER entity or the transitional ER exit sites for dual labeling with peroxisomes. For whole ER we used the translocon subunit SEC61A1. Human SEC61A1 cDNA was obtained from ASUS repository (Arizona State University, clone HsCD00350497) and subcloned by PCR into the EGFP

C1 vector between SalI and KpnI using primers SEC61A Forw and Sec61A Rev (sequences in **Supplementary Table 1**). For the labeling of transitional ER exit sites we used the Sec16B-GFP[36] (pmGFP-Sec16S) chimera (obtained from Addgene).

Labeling of mitochondrial subunits with fluorescent proteins was performed by tagging the precursors at the C terminus. The outer mitochondrial membrane was labeled with the human Tom20 subunit of the translocator with mCherry and for mitochondrial nucleoids we used the mouse mitochondrial transcription factor A (TFAM). Untagged cDNAs were obtained from Origene and the coding sequences were PCR amplified digested with BglII and SacI and subcloned in frame into pmCherry-N1 or EGFP-N1 vectors (Clontech). For PCR amplification we used primers Tom20 Forw, Tom20 Rev, TFAM Forw and TFAM Rev (sequences in **Supplementary Table 1**).

Rab8A tagged with Cherry was a kind gift of L. Maldonado-Baez (NHLBI, NIH). H-Ras was obtained from a cDNA library created from MRC-5 human lung fibroblasts by RT-PCR procedures using the Superscript kit (Life Technologies) and the following primers: H-Ras Forw TTCGAATTCAGAGGAGCGATGACGGAATATAAGCTGGT; H-Ras Rev GGTGGATCCCGGGGTGACTGGGCTCCAGCAG. The cDNA was cloned in frame between EcoRI and BamH1 in the EGFP C1 vector tagging the molecule at the N terminus.

Bead and fluorescent slide samples. Bead samples were prepared as previously described[13] except that we mounted the beads in the immersion oil used for each microscope. When conducting optical sectioning experiments (**Supplementary Fig. 13**) we acquired z stacks of a yellow-green, thick fluorescent plastic slide (Chroma Technology, 92001).

Cell culture and cellular sample preparation. Routine cell culture procedures were followed, keeping cells in DMEM supplemented with 10% FBS (Life Technologies) in a CO_2-supplied incubator (5%) at 37 °C. Experiments were performed in a human transformed cell line designated as MRL-TR. This line was derived from primary lung MRC-5 fibroblasts (ATCC). For live imaging, cells were plated in either four-well chambers (Labtek II) with coverglass bottoms or in Bioptechs dishes (no. 1.5 glass thickness in either case). DMEM supplemented with 10% FBS (without phenol red) was used as the imaging medium in all live cell experiments. Data collection for **Figures 2** and **4** and **Supplementary Videos 1–9** and **11** was performed at room temperature. For ER experiments (**Fig. 3** and **Supplementary Video 10**), we used a Bioptechs Delta T system to perform experiments at 37 °C.

Comparative confocal microscopy. We performed line-scanning confocal imaging on a Live 5 duoscan microscope (Zeiss) equipped with galvanometric scanning mirrors and 488-nm (for GFP excitation) and 561-nm (for Cherry excitation) diode lasers. A Planapo 100× oil immersion lens with 1.46 NA (Zeiss) was used for line-scanning confocal imaging. The confocal aperture was set to 1 AU for both colors, Kalman averaging was set to 2 and scanning speed ranged from 20 to 40 frames per second (f.p.s.) depending on the intensity of the signal. To obtain imaging speeds equivalent to instant SIM, scanning was performed at a field of view of 512 × 512 pixels, yielding a pixel size of 130 nm. Acquisition was simultaneous with appropriate pre-acquisition

single channel corrections for cross excitation, bleed through and saturation. A 565-nm RTNT1 NFT dichroic mirror was used to split emitted light and direct it into appropriate acquisition channels using a BP 495–555-nm (band-pass) filter for GFP emission and a LP 580-nm (long-pass) filter to detect signal from mCherry. For z stacks, a piezo focus lens positioner (Physik Instrumente, P-725.2CD and E-665) was used to obtain 250-nm axial steps, thus obtaining 12 slices (for 3-μm depth, identical to instant SIM imaging).

Spinning-disk confocal imaging was performed on a TE2000 microscope stand (Nikon) equipped with a charge-coupled device (Photometrics CoolSnap HQ2) and CSU-X10 spinning disc confocal head. Images were acquired using a 60×, 1.49 TIRF objective (Nikon), with exposure times of 20–50 ms per frame. Imaging volumes were acquired using a piezoelectric stage (Mad City Labs). All hardware was controlled with MetaMorph (Molecular Devices).

When performing comparative spinning-disk, line-scanning confocal experiments, and instant SIM experiments (**Fig. 2**, **Supplementary Fig. 11** and **Supplementary Videos 1**–**3**), we fixed the imaging volume thickness (3 μm) and number of time points (20) and adjusted laser power to produce the brightest signals we could without overly bleaching the sample.

Zebrafish embryo sample preparation. For live zebrafish imaging, *Tg(XlEef1a1:dclk2-GFP)io008* embryos[13] were collected by natural spawning and maintained at 28 °C. Before imaging, embryos at 72–78 h after fertilization were anesthetized in Tricaine (Sigma, E10521) at a final concentration of 600 mM in embryo media (60 mg RedSea Coral Pro Salt (Drs Foster and Smith Pet Supplies) per liter ddH$_2$O). Anesthetized embryos were immobilized in 0.75% low-melt agarose (Cambrex, 50080) on 25 mm no. 1.5 round coverslips (Warner Instruments, 64-0715), placed in a round coverslip holder (ASI, I-3033-25D) and imaged at room temperature.

32. Oliphant, T.E. Python for scientific computing. *Comput. Sci. Eng.* **9**, 10–20 (2007).
33. Richardson, W.H. Bayesian-based iterative method of image restoration. *J. Opt. Soc. Am.* **62**, 55–59 (1972).
34. Lucy, L.B. An iterative technique for the rectification of observed distributions. *Astron. J.* **79**, 745–754 (1974).
35. Goedhart, J. *et al.* Structure-guided evolution of cyan fluorescent proteins towards a quantum yield of 93%. *Nat. Commun.* **3**, 751 (2012).
36. Bhattacharyya, D. & Glick, B.S. Two mammalian Sec16 homologues have nonredundant functions in endoplasmic reticulum (ER) export and transitional ER organization. *Mol. Biol. Cell* **18**, 839–849 (2007).